

The distribution and variability of low-level cloud in the North Atlantic trades

L. Nuijens,* I. Serikov, L. Hirsch, K. Lonitz and B. Stevens

Max Planck Institute for Meteorology, Hamburg, Germany

*Correspondence to: L. Nuijens, Max Planck Institute for Meteorology, Bundesstrasse 53, 20146 Hamburg, Germany.
E-mail: louise.nuijens@mpimet.mpg.de

In the North Atlantic trades, variations in the distribution of low-level cloud are rich. Using two years of observations from a remote-sensing site located on the east coast of Barbados, the vertical distribution of cloud and its contribution to low-level cloud amount are explored. The vertical distribution of first-detected cloud-base heights is marked by a strong peak near the lifting condensation level (LCL) from passive optically thin shallow cumuli. Cloud with a base near this level dominates the total cloud cover with a contribution of about two-thirds. The other one-third comes from cloud with its cloud base further aloft at heights > 1 km, such as cumulus edges or stratiform cloud below the trade inversion. Cloud found aloft, regardless of where its base is located, contains more variance, in particular near the inversion and on time-scales longer than a day. In turn, cloud near the LCL is surprisingly invariant on longer time-scales, although consistent with existing theories. Because this component does not systematically vary, changes in cloud cover in response to changes in meteorology or climate may be limited to changes in its contribution from cloud aloft.

Key Words: trade-wind cumulus; ground-based remote sensing; cloud amount; transition layer

Received 19 March 2013; Revised 23 November 2013; Accepted 25 November 2013; Published online in Wiley Online Library 18 February 2014

1. Introduction

In regions where the ocean surface is warm and large-scale subsiding motion is moderate to weak, the vast majority of marine low-level cloud is shallow cumulus. The trades for instance are famous for their shallow 'trade-wind' cumuli. But also deeper into the Tropics, within the InterTropical Convergence Zone (ITCZ), deep convection is regularly preceded and followed by fields of shallow cumulus (Malkus and Riehl, 1964; Johnson and Lin, 1997; Sui *et al.*, 1997). Because of their widespread occurrence, and therefore large statistical weight, shallow cumuli have a non-negligible impact on the short-wave radiation budget, and hence on climate (Bony and Dufresne, 2005; Vial *et al.*, 2013). However, estimating their radiative effect in a global climate model remains a challenge. For instance, the amount of low-level cloud in the trades, even in simulations of the current climate, ranges between 10 and 40% and the cloud field can have a very different vertical structure depending on the model version (Medeiros and Stevens, 2011; Qian *et al.*, 2012). Therefore, predicting how the distribution of cloud may change as the climate warms, and how those changes impact the planetary albedo, is still subject to many uncertainties.

The difficulty in simulating broken cumulus fields is not just because the typical sizes of cumuli make up only a fraction of a model grid box, but also because their relationship to the large-scale environment is subtle. Understanding how shallow cumuli relate to the thermodynamic structure of the environment and the

large-scale forcing has advanced much through the use of Large-Eddy Simulation (LES), which explicitly resolves flows over grids with meshes as fine as 10 m or less. Such simulations have also been a great tool for developing and testing parametrizations in climate models. However, most LES studies use an idealized set-up of the large-scale environment, so that there is much left to be learned about the variability of cumulus fields under the wide range of conditions experienced in nature. For instance, what are robust features of the vertical structure of low-level cloud that models should be able to reproduce? What features of clouds are most sensitive to changes in the environment and have the largest variability? Between different LES codes, cloud amount also differs as much as it does among climate models (10–40%), related to the different schemes used to represent advection, microphysics and sub-grid turbulence, which shows that resolution alone is not the only issue (Matheou *et al.*, 2010; Van Zanten *et al.*, 2011).

Since the early field explorations by Malkus and Riehl (1964), who linked cloud distributions over the Pacific from photographs to synoptic weather patterns, few studies have attempted to connect the structure and behaviour of trade-wind cumulus fields to the large-scale flow (Slingo, 1978). In part, this is because field studies in the trades are rare, and the few field studies that did take place often lacked the instrumentation needed to characterize the macro-physical structure of clouds over a large area and over a longer period of time. The most recent Rain In Cumulus over the Ocean campaign (RICO; Rauber *et al.*, 2007)

lasted for almost three months and deployed a scanning K-band radar, but nonetheless failed to produce accurate statistics of the cloud field because of clutter issues.

Advances in space-borne remote sensing have in turn made it increasingly feasible to characterize cumulus fields over larger areas in more detail (Zhao and Di Girolamo, 2007), even though passive remote-sensing instruments still suffer from the small spatial scales and low optical depths of shallow cumulus, as well as from the presence of mid- and high-level cloud that can obscure underlying low-level cloud (Zhao and Di Girolamo, 2006; Marchand *et al.*, 2010). Especially the active radar and lidar instruments launched in 2006, CloudSat and CALIPSO (Cloud-Aerosol Lidar and Infrared Pathfinder Satellite Observation), have demonstrated good skill in observing the vertical structure of low-level cloud (Medeiros *et al.*, 2010; Ahlgrimm and Kohler, 2010; Leahy *et al.*, 2012). However CloudSat and CALIPSO are not that well suited for studying variability in the distribution of cloud on time-scales much shorter than a month, because their sampling at a specific location is infrequent.

The need for better observations of marine boundary-layer clouds to evaluate and complement modelling studies has in past years motivated the installation of long-term measurement sites. After a successful 19-month long campaign in the Azores using the Department of Energy (DOE) Atmospheric Radiation Measurement (ARM) mobile facility (Remillard *et al.*, 2012), DOE is installing a permanent ARM site at that location focused on observing the high cloud fraction regime of stratocumulus-topped boundary layers. Deeper into the subtropics, where the low cloud fraction broken trade-wind cumulus fields prevail, the Max Planck Institute for Meteorology in collaboration with the Caribbean Institute for Meteorology and Hydrology has installed the Barbados Cloud Observatory (BCO), a platform with remote-sensing instruments similar to that of the ARM sites (Xie *et al.*, 2010), including a cloud radar, multi-channel Raman lidar, ceilometer and micro-rain radar. The site is located on an eastward promontory of the island of Barbados (13°N, 59°W), facing the North Atlantic and is therefore fully exposed to the undisturbed trade winds. The long temporal record (over 3 years and continuing) ensures that a wide range of conditions are captured. Both suppressed convection in the dry season and more vigorous convection in the wet season are common, and it is therefore an interesting location from the perspective of climate uncertainties, which are particularly large for clouds in moderately subsiding regimes.

A two-year dataset collected at the BCO is presented and discussed here to help build a better understanding of the distribution and variability of cloud in this regime. After a description of the data used to derive statistics of clouds and rain (section 2), we address the following questions: what is the vertical distribution of low-level cloud from simple and more sophisticated instruments? (sections 3.1–3.2); how do different components of the cloud field vary and on what time-scales? (section 3.3); and how does this affect the seasonality of cloudiness over a two-year period? (section 4). Our results are summarized and concluded in section 5.

2. Data and methods

2.1. The Barbados Cloud Observatory

The Barbados Cloud Observatory is located on Deebles Point, a site on the east coast of Barbados facing the Atlantic Ocean*. The site has been in continuous operation since 1 April 2010, and is ongoing. The instruments used in this study are two lidar systems: a laser ceilometer and a multi-channel Raman lidar, and two radar systems: the micro-rain radar (MRR) and a scanning cloud radar (KATRIN). The ceilometer and Raman lidar are

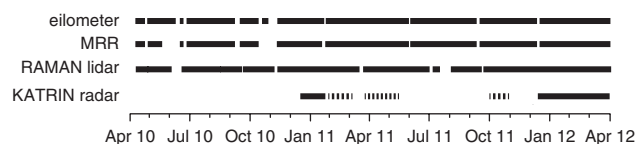


Figure 1. Instrument uptime during two years of measurements. Solid lines indicate the vertical pointing mode, and dotted lines indicate the scanning mode, during which vertical pointing and scanning at different elevation angles (Plan Position Indicator scanning) alternate.

used to derive the vertical distribution of cloud-base heights, and cloud cover, whereas the radar is used to derive a vertical profile of hydrometeor (cloud and rain) fraction. The MRR mainly serves to provide a rain flag. Because the ceilometer and MRR have the most continuous data record to 1 April 2012 (Figure 1), they are the key data source for our analysis. The Raman lidar has a long data record, but closes its hatch for 1 h every day when the sun is overhead and when it rains. Although the ceilometer and MRR have less power and fewer options than the lidar and radar, they are cheaper and easier to maintain, and hence are particularly attractive because the analysis could be easily extended to other climate regimes where such simple instruments operate. The cloud radar is used to support the ceilometer and MRR results for shorter periods of time.

2.1.1. Ceilometer

The Jenoptik laser ceilometer measures backscattered energy from aerosols and cloud droplets using a 1064 nm wavelength, and is sensitive to the concentration of particles as well as their surface area. The ceilometer has been deployed with two versions of its laser optical unit: the newer 15k-X version has a larger field of view of 1.7 mrad instead of 0.4 mrad used by the 15k version. The 15k-X is found to have less accurate results during daytime hours, when background noise increases, especially at the low sun zenith angles at this latitude. It was therefore only used when the 15-k optical unit was broken (16 December 2011 to 9 March 2012). The temporal resolution of backscatter profiles is 30 s, with a 15 m resolution up to a range of 15 km (but results are only used up to 4 km).

2.1.2. Micro-rain radar

The MeTeK micro-rain radar (MRR) is a vertically operating 24 GHz frequency-modulated continuous-wave (FMCW) radar that uses the Doppler shift (frequency shift between the transmitted and received signal) to measure the falling velocity of rain drops and from this derives the drop size distribution, utilizing the known relation between fall velocity, raindrop size and scattering cross-section. Upon integration of the raindrop size distribution, the rain-rate, as well as other moments, are derived. Values of the rain rate below 0.03 mm h^{-1} are, according to the noise level, assumed to be below the sensitivity of the system, and are thus interpreted as zero. The MRR operates at a 1 min resolution, with a range gate of 30 m up to 3 km.

2.1.3. Raman lidar

The in-house developed Raman lidar measures backscatter return from atmospheric molecules, aerosols and cloud droplets as a response to laser pumping at three wavelengths (1064, 532, 355 nm). The lidar products used are the particle backscatter coefficient at 532 and 355 nm derived with the pure rotational Raman lidar technique, and the particle depolarization ratio measured at 532 nm. Vertical profiles of these products are averaged over 2 min at a 60 m resolution up to 15 km. The lidar hatch closes for 1 h (1530–1630 UTC) when the sun is directly overhead and during periods of rain which are identified

*<http://barbados.mpimet.mpg.de> (accessed 20 December 2013).

when the MRR measures rain-rates $> 0.05 \text{ mm h}^{-1}$ at any height below 3 km.

2.1.4. KATRIN cloud radar

The KATRIN radar is a scanning Ka band (36 GHz) Doppler radar with two receiver channels that provides profiles of reflectivity at two linear polarizations as well as other information derived from the Doppler spectra. The radar reflectivity is a function of the diameter of particles to the power six as well as their concentration. At this frequency, the smallest detectable particles are cloud droplets, but also larger rain drops are observed, and in the case of heavy rain, the radar beam can attenuate. The raw data has undergone an intensive filtering procedure to exclude erroneous returns due to clutter and to a smaller extent atmospheric plankton. The filtering routine utilizes combinations of all four measured quantities (reflectivity, Doppler velocity, spectral width and linear depolarization ratio) together with temporal and spatial cluster analyses. Only data from the vertical pointing mode are used here to derive cloud statistics, which include a profile every 10 s with a resolution of 30 m up to 15 km. No data are used at heights below 300 m, where the signal to noise ratio is insufficient for a proper measurement of hydrometeors.

2.2. Deriving cloud and rain statistics

Cloud-base heights and a cloud mask are derived using ceilometer and lidar backscatter profiles and radar reflectivity profiles, as described below. A rain flag is derived from the MRR rain-rate profiles. For each instrument, the original temporal resolution is maintained, but the cloud mask is gridded onto a common height grid that has a 60 m resolution in the vertical. Profiles are only analyzed up to a height of 4 km, so that the data include primarily low-level cloud such as shallow cumulus and stratiform cloud, but may include cases of deeper convection.

The ceilometer is used only to detect the height of the first cloudy point (cloud base), because its signal attenuates quickly after cloud penetration. The standard ceilometer software provides an estimate of cloud-base height, but these data are found to be unreliable during daytime hours, presumably because the fixed threshold used to identify cloud is below the background noise. Instead we make use of the vertical gradient between the expected and actual background noise. If $P(r)$ is the raw backscatter signal in photon counts at range gate r , then the expected background noise level can be estimated as

$$P^*(r) = P(r) + \sqrt{P(r)},$$

where $\sqrt{P(r)}$ is a standard error, assuming perfect Poisson statistics. If after smoothing $\ln[P(r)r^2]$ exceeds the expected $\ln\{P^*\{r - \Delta r\}(r - \Delta r)^2\}$ at a level Δr below it, which happens when $\ln[P(r)r^2]$ sharply increases, and it does for two consecutive range gates, cloud-base height is taken as the lower of the two range gates. Profile smoothing is performed by applying an unweighted running average over 180 m and Δr is taken to be 60 m. Each first detected cloud-base height (cbh^1 , where the superscript ¹ denotes it is the first detected base, rather than the second or third) from the ceilometer (shown as black dots in Figure 2(a–c)) is matched with the corresponding MRR rain flag (Figure 2(d)) to identify those cbh^1 that may be contaminated by rain. The rain flag is 1 when rain rates $> 0.05 \text{ mm h}^{-1}$ are present in at least five range gates of a MRR rain profile, which do not need to be consecutive.

The cloud mask from the Raman lidar data (Figure 2(c), dark green contours) is derived from the profiles of particle backscatter β at 355 and 532 nm (Figure 2(b)). Pixels are cloudy when β_{355} and β_{532} exceed $30 \text{ M m}^{-1}\text{sr}^{-1}$, and when the error in β_{355} and β_{532} is less than 30%. Single isolated cloudy pixels are excluded. The value of $30 \text{ M m}^{-1}\text{sr}^{-1}$ is subjectively chosen to ensure that profiles with a high aerosol load, such as dust (which typically sits at heights $> 1 \text{ km}$, within the cloud layer) or hygroscopic aerosol

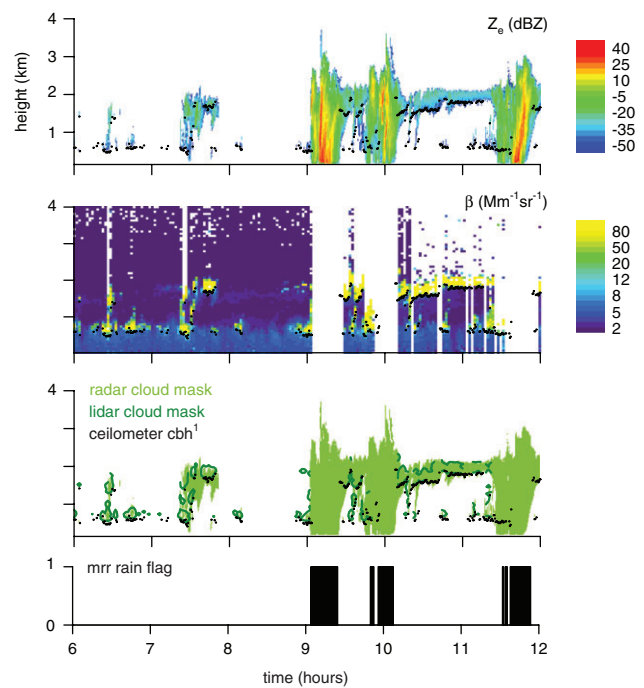


Figure 2. (a) Reflectivity Z_e from the KATRIN radar, (b) particle backscatter β_{532} from the Raman lidar, (c) cloud masks from the KATRIN radar and the Raman lidar and (d) the rain flag from the MRR for 21 January 2012, 0600–1200 UTC. Black dots in (a)–(c) represent the first detected cloud-base height cbh^1 from the ceilometer.

just below cloud base are not misidentified as cloud. An additional check has been done ensuring that the depolarization ratio δ of the cloud mask (not shown) has values typical for cloud droplets i.e. $\delta < 0.05$. A $\delta = 0.05$ seems high for spherical droplets (that principally do not change the polarization), but such a value is reached when multiple scattering in clouds occurs. Note that, when the MRR rain flag is 1, β_{532} in Figure 2 is missing, because the Raman lidar hatch is closed during times of rain (and for a continuing 3 min after the last rain detection) using the same MRR criterion.

The cloud mask from the KATRIN radar data (Figure 2(c), light green contours) is derived by setting a threshold of -40 dBZ on the equivalent radar reflectivity Z_e (Figure 2(a)). This threshold is rather restrictive, but subjectively chosen by visually inspecting that returns from clutter and atmospheric plankton are excluded. Most of that clutter at specific height levels is evident at $Z_e < -40 \text{ dBZ}$ and cannot be removed with a more advanced LDR filtering algorithm because of poor behaviour of the radar cross-channel before February 2012. During the months February and March of 2012, a more sophisticated clutter filter allows interpretation of results from the radar at $Z_e < -40 \text{ dBZ}$ meaningfully.

3. The vertical distribution of cloud

The simplest measure of cloudiness can be derived from the ceilometer, which provides the height of the first detected cloud base cbh^1 . It thus provides a temporal cloud cover CC that is defined as the fraction of time that a cloud-base height is overhead. As will be shown, much of the variability in the cloud field can be inferred by studying the vertical distribution of cloud-base heights, and its inferred cloudiness, alone. That is particularly useful because the ceilometer has the longest continuous record and is overall a relatively cheap system to operate. In this section we first explore the vertical distribution of cloud bases from the ceilometer and then use the cloud radar, which measures a full profile of cloud, to demonstrate that the ceilometer, despite its simplicity, reveals much about the variability in the total cloud field.

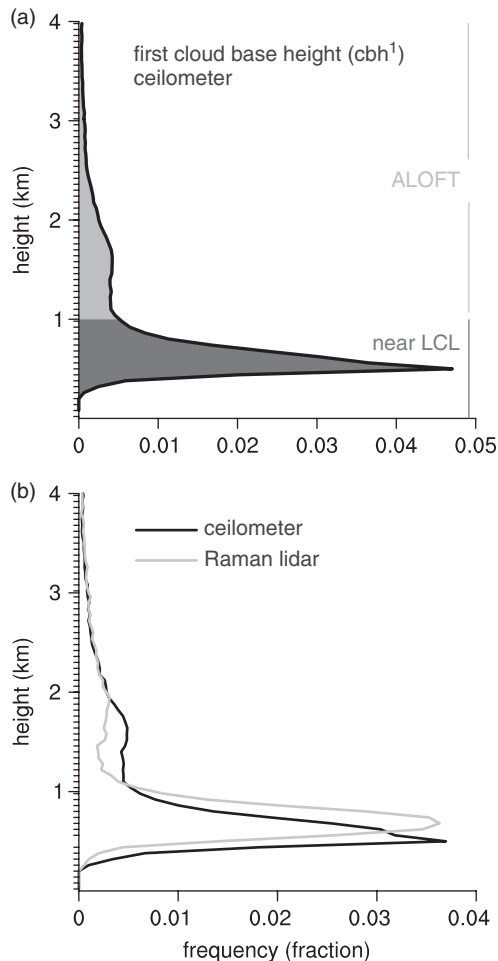


Figure 3. (a) Frequency distribution of first detected cloud-base height cbh^1 from the ceilometer for 1 April 2010 to 1 April 2012 (Δz of bins = 60 m, indicated by the minor tickmarks). The dark and light grey shaded areas correspond to detections below 1 km (near the LCL) and detections above 1 km (ALOFT). Only non-raining cloud is included, because during periods of rain (7% of the total period) the cbh^1 cannot always be accurately determined. (b) Frequency distribution of cbh^1 from the ceilometer (black) and lidar (light grey) from 1 December 2010 to 31 May 2011 and 1 September 2011 to 31 March 2012.

3.1. Cloud-base height distribution and cloud cover

The majority of cloud-base heights shown in Figure 3(a) is found close to the lifting condensation level LCL, which is estimated at 700 ± 150 m using temperature and humidity measurements performed at 25 m asl at a nearby tower on Ragged Point. The spread in the vertical distribution of cloud bases around 700 m reflects the range in LCL from drier days in winter to moister days in summer. Above about 1 km, detections of cbh^1 are less frequent and include contributions from sides of clouds that are irregular or sheared by vertical gradients in the mean horizontal wind, cloud fragments from maturing cumuli that have lost their connection to the sub-cloud layer, or stratiform-like cloud. Such a profile appears a general feature of trade-wind cumuli and is hinted at by earlier studies using airborne or space-borne lidar systems (Nuijens *et al.*, 2009; Medeiros *et al.*, 2010).

Motivated by the idea that the mechanism that regulates cloud at different heights is different, cloud detections below and above 1 km are referred to separately as cloud near the LCL using the subscript LCL (dark grey shading) and cloud aloft using the subscript $ALOFT$ (light grey shading). The first, as its name indicates, is regulated by the location of the LCL with respect to the transition layer, or in theories of deep convection a layer of convective inhibition (CIN), which is a small layer atop the mixed layer wherein absolute humidity decreases and potential temperature increases. Once a cloud has formed, its ability to grow deeper beyond 1 km or laterally spread aloft depends on a number of other factors, such as entrainment, subsidence, the

temperature and humidity gradients in the cloud layer, and the presence of inversions.

Total cloud cover CC can be derived by summing the fraction of cbh^1 per height bin from 0 to 4 km. Summation up to 1 km gives the contribution of cloud near the LCL to cloud cover (CC_{LCL}), whereas summation from 1 to 4 km gives the contribution of cloud aloft to cloud cover (CC_{ALOFT}). For two years of data, we obtain a CC equal to 0.31, with about two-thirds coming from CC_{LCL} ($= 0.21$) and one third coming from CC_{ALOFT} ($= 0.1$). Cloud aloft only contributes effectively to cloud cover when there is no cloud base below 1 km. The relative contributions of CC_{ALOFT} and of CC_{LCL} thus change if the cloud field is viewed from space instead. The one advantage of viewing clouds from the surface is that the surface buoyancy flux is naturally the source of energy for cumulus clouds, so that it allows one to separate the part of the cloud field with roots in the sub-cloud layer, e.g. with a cloud base near the LCL, from clouds that are disconnected from sub-cloud layer thermals. Note that cloud detections at mid and high levels are not considered here, and because cirrus layers are frequent at this location (Brück, 2013), the derived cloud cover is an underestimation of the total cloud cover.

An important point to mention is that these numbers represent only the non-raining part of the cloud field. Although the ceilometer can detect a cloud-base height in light rain events, such estimates will be increasingly biased as the rain intensity increases, and are not detectable during heavy rain. Here in only 39% of the rain events a cloud-base height is detected, with 62% of those bases located below 1 km and 38% above 1 km. The ratio of cloud aloft to cloud near the LCL during relatively light rain events, when a cbh^1 can be detected, is thus comparable to the non-raining part of the cloud field. Because during the remaining 61% of heavier rain events the relative ratio of cbh^1 below and above 1 km cannot be assessed, the raining part of the cloud field is overall treated as a separate contribution. With a rain cover of $RC = 0.07$, the total period of time with either cloud or rain overhead is thus $0.31 + 0.07 = 0.38$ (Table 1). The radar estimate of total cloud and rain cover is not very different (next section) and thus Barbados appears a quite cloudy place.

The distribution of cbh^1 from the ceilometer can be evaluated using the Raman lidar during periods of simultaneous operation (Figure 3(b)). Here the ceilometer distribution (in black) has slightly different frequencies, because of the different observation period used, from 1 December 2010 to 31 May 2011 and 1 September 2011 to 31 March 2012. The Raman lidar distribution (light grey) is similar, but its distribution below 1 km is somewhat broader, there are fewer detections between 1 and 2 km, and all cloud bases are elevated by about 250 m. The lower temporal resolution of 2 min, versus 30 s of the ceilometer, leads to an overall smearing out of the cloud field and is responsible for the broader distribution and larger cloud cover CC (Table 1). At the same time, the low temporal resolution causes very thin cloud or irregular edges of cloud to be missed between 1 and 2 km, and therefore the relative contribution of CC_{ALOFT} to CC is smaller.

The cloud cover and relative contribution of CC_{LCL} and CC_{ALOFT} also depend on the threshold on particle backscatter that is used to detect cloud. Here, the threshold is somewhat conservative ($30 \text{ M m}^{-1} \text{ sr}^{-1}$) to ensure that aerosol is not misidentified as cloud. Lowering the threshold, which is equivalent to increasing the amount of optically thin cloud, would increase CC and CC_{LCL} and further reduce the ratio of CC_{ALOFT} to CC_{LCL} (Figure A1 and its discussion in the Appendix). The $30 \text{ M m}^{-1} \text{ sr}^{-1}$ threshold also determines the peak in cbh^1 , i.e. upon lowering the threshold to $10 \text{ M m}^{-1} \text{ sr}^{-1}$, the height of the peak cloud fraction and median cbh^1 shift to 500 m (not shown). Because the ceilometer cbh^1 is derived using a gradient method, rather than a threshold method (section 2.2), it is less sensitive to variations in background noise, sunlight or aerosol load, and therefore is used as our main data source in the remainder of the analysis.

Table 1. Total (projected) low-level cloud cover CC and its various contributions: from cloud at heights < 1 km (CC_{LCL}), rain (RC), and cloud at heights > 1 km (CC_{ALOFT}). The radar (all hydrometeor) estimate under CC_{LCL} represents both cloud and rain, and is thus a combined $CC_{LCL} + RC$. For the ceilometer + mrr two years of data are used (Figure 3), whereas for the radar and lidar only the months February and March of 2012 are used, during which a more sophisticated clutter filter was employed that allows for interpretation of results from the radar at $Z_e < -40$ dBZ meaningfully.

Instrument	CC_{LCL}	RC	CC_{ALOFT}	CC
Ceilometer (+ mrr)	0.21	0.07	0.1	0.38
Lidar	0.36	–	0.09	0.45
Radar (all hydrometeors)	0.27	–	0.13	0.40
Radar (rain filtered)	0.18	–	0.12	0.30

3.2. The radar view on the vertical cloud distribution

To get more insight into what is behind the distribution of cloud bases as seen by the ceilometer, the cloud radar data are explored. Unlike the ceilometer and lidar, the radar beam does not attenuate in optically thicker cumulus cloud, unless very heavy rainfall is encountered. It thus provides a full profile of the fraction of cloud and rain returns, together referred to as hydrometeor returns, plotted as a solid grey line in Figure 4. For the $Z_e = -40$ dBZ threshold used here, hydrometeors between 750 m and 2 km have a frequency of occurrence of about 0.13. A qualitatively similar profile is observed when using only periods without heavy rain, indicated by the dashed line. This profile disregards periods during which the MRR rain mask is 1 (section 2.1.2) and the ceilometer is not able to detect a cloud base, indicative of heavy rain. For the remaining data, all returns below the detected cbh^1 are masked. These returns are due to drizzle that is not strong enough to be detected by the MRR, or that has evaporated before reaching the surface (Comstock *et al.*, 2004). This still leaves a frequency of 0.04 at heights near 300 m, which, given that the LCL is on average 700 ± 150 m, must be partly a result from the cbh^1 being low biased in cases of light rain.

A first maximum in hydrometeor returns is found just below 1 km, which corresponds to the height where most cloud bases are found. These cloud bases from the radar are artificially higher than what the ceilometer and lidar observe due to the conservative Z_e threshold, which effectively removes cloud near its base, where liquid water content is lower than towards cloud top. There is a hint of a second maximum in returns just below 2 km, which is where the top of the cloud layer or the base of the trade inversion is located. As will be shown in the next section, this second peak marks a stratiform cloud layer that resembles the simulation results obtained by the LES intercomparison study of trade cumuli under somewhat stronger inversions, as observed during the Atlantic Trade Wind Experiment (ATEX) near 12°N , 35°W in 1969 (Augstein *et al.*, 1973; Stevens *et al.*, 2001). This regime with stratiform cloud near cumulus cloud tops is thought to be an intermediate regime, between the upstream high-cloud fraction regime with shallow boundary layers capped by strong inversions and the downstream low-cloud cover regime in deeper boundary layers under weaker inversions. In their study of cloud-base and cloud-top distributions over the Pacific as seen by the space-borne CALIPSO lidar, Leahy *et al.* (2012) also find a pronounced mode of cloud near 2 km in a region (15°S , 155°W) classified as a broken cumulus regime. Apparently even this far into the Tropics (Barbados is located at 13°N , 59°W) stratiform cloud layers are not an uncommon phenomenon.

The total cloud cover and the ratio between cloud near the LCL and cloud aloft derived from these radar profiles are similar to what is found for the ceilometer, even though the radar sees less cloud near the LCL because of the conservative threshold (Table 1). Had we used a less conservative threshold,

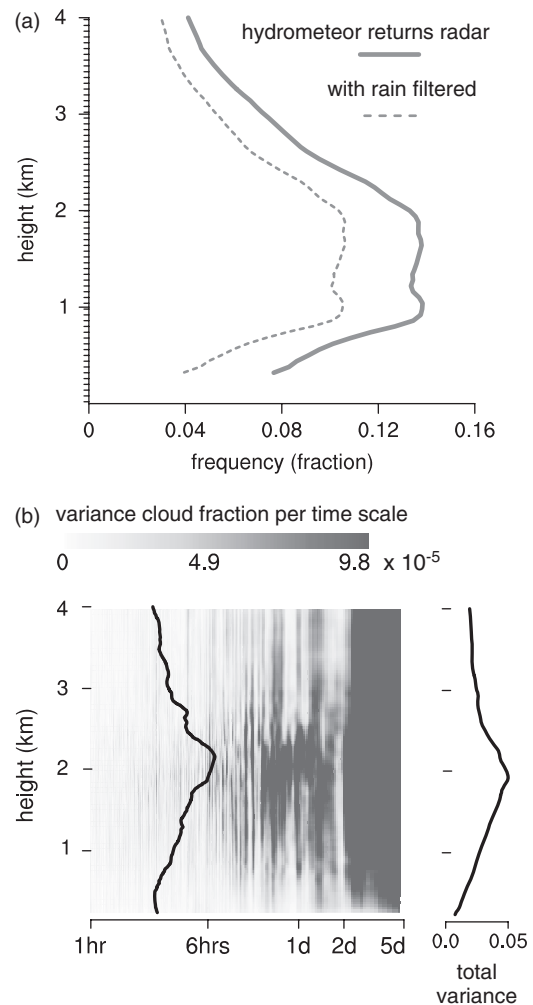


Figure 4. (a) Frequency distribution of radar returns of hydrometeors (both cloud and rain; solid grey) and radar returns for periods without significant rain (dashed grey), for the periods 1 December 2010 to 31 May 2011 and 1 Sept 2011 to 31 March 2012. The rain-filtered profile is created by excluding profiles where the MRR rain mask equals 1 but no cloud-base height is detected (which are significantly strong rain-rate events). For the remaining profiles, all returns below the detected cloud-base height are masked. (b) On the left the variance of the cloud-only returns is plotted (grey contours) as a function of height and time-scale, for the period 1 January 2012 to 31 March 2012. The superimposed dark line indicates the time-scale that explains 50% of the variance. The total variance per height level is plotted on the right.

the amount of optically thin cloud near the LCL would increase and further reduce the ratio of CC_{ALOFT} to CC_{LCL} (Appendix). However across a range of thresholds the dominant contributor to CC remains cloud near the LCL, whether as optically thin shallow cloud or as thicker raining cloud.

Note that, even though the profile of hydrometeor fraction is halved when excluding periods with significant rain, the total projected cloud cover CC reduces only by a quarter from 0.4 to 0.3. This means that the non-raining part of the cloud field has less vertical coherence than the raining part of the cloud field. Indeed, the overlap ratio calculated by dividing the cloud fraction defined by volume, which is the vertically averaged profile of Figure 4, by the cloud fraction defined by area, which is the projected cloud cover CC in Table 1, equals 0.31 for the hydrometeor profile and 0.19 for the rain-filtered profile. That the cloud overlap in a cumulus cloud field is small is due to the high irregularity of cumulus clouds over a wide range of scales, which has been shown by Neggers *et al.* (2011). For that reason, it is also not surprising that a third of the cbh^1 of non-raining cloud is found at heights above 1 km. Also for periods with light rain, when cbh^1 can be detected, more than a third of those are located aloft. It is indeed not uncommon when in the trades to observe rain falling out of the tops of slanted and fragmented cumuli that are in a decaying stage of their life cycle. To get more insight into

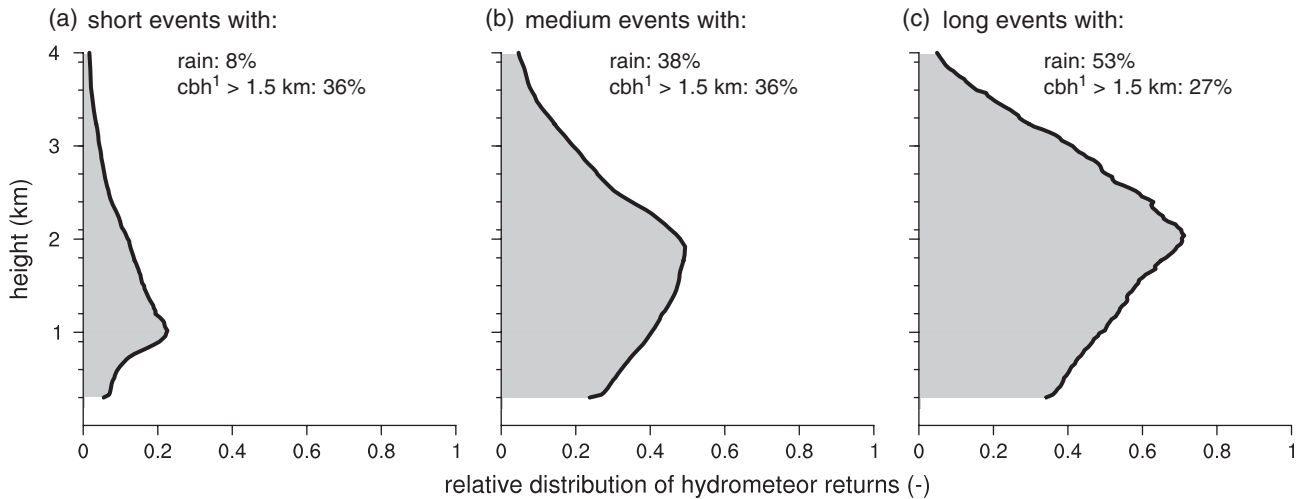


Figure 5. The vertical distribution of radar hydrometeor returns relative to the total duration of cloudy sky, for cloud passages (a) < 3 min (contributing 37% of the total length of cloudy sky), (b) 3–12 min (57%) and (c) > 12 min (6%). The profile is created by averaging all individual profiles of hydrometeor duration divided by projected duration within each composite. Also denoted is the percentage of entities with rain near the surface and the percentage of entities that have their minimum cbh^1 located above 1.5 km.

the nature of different clouds, the vertical distribution of radar returns is analyzed separately in the following section for each cloud entity that passed the site.

3.3. Distribution by cloud entity and cloud duration

Different clouds within a cloud field can be characterized by their different overpass time or durations. The cloud duration does not translate directly into a cloud size, because clouds do not necessarily pass an instrument along their longest axes. The distribution of cloud durations may therefore be biased towards smaller cloud sizes. This is true for both small and large clouds, however, so that for a large enough sample of cloud passages, and the assumption of isotropy in the cloud field (Hinkelman *et al.*, 2005), which given the persistent wind direction from the east is not unreasonable, the separation of short from long clouds may be meaningfully interpreted.

For the radar data, the duration of each separate cloud entity is used to identify short, medium and long cloud passages, where a cloud entity consists of those radar pixels that have common edges and vertices. Cloud entities less than 30 s long are omitted. A cloud entity can include both cloudy or rainy pixels, so even if the following text refers to a cloud entity or cloud duration, this applies to all hydrometeors. By normalizing the cloud duration at each height by the duration or width of the cloud entity projected onto the surface, a profile is derived that represents the relative distribution of hydrometeors within each entity. These fractions can range from 0 to 1, for instance perfectly upright cylindrical clouds would have a fraction of 1, but as the cloud cylinder tilts in the along-wind direction, this number decreases. Because hydrometeor returns at different heights can overlap, the fractions do not sum to 1, and the height-averaged fraction is thus a measure of the effective overlap within each cloud entity. The profiles of hydrometeor fraction are combined into composites for entities that are either < 3 , 3–12 and > 12 min in duration and then averaged over height. These are shown in Figure 5. By averaging the normalized profiles, rather than first summing the duration of all clouds and then dividing by the total cloud duration, the structure of individual entities is better preserved. Remember that, because clear-sky profiles are not taken into account, these profiles do not provide information on real hydrometeor fractions such as in Figure 4.

It is clear that the average distribution for a field of short-lasting cloud overpasses is different from that of long-lasting cloud overpasses, and decreases with height above cloud base more often so than Figure 4 would suggest. Thirty six percent of the cloud entities that are defined as short are located entirely at

heights beyond 1.5 km, because their minimum cbh^1 is > 1.5 km (where 1.5 km is chosen instead of 1 km to account for the unrealistic high cloud bases of the radar –the discussion based on Figure 4 –and to target the stratiform layer near 2 km). These 36% are likely cloud patches disconnected from the surface and decaying cloud. Because the short events have such a fragmented and tenuous nature, the effective overlap of the cloud field as a whole is small –note that the values on the x-axis are relative to the total projected duration of cloudy sky. As clouds get longer and wider they also get deeper and more frequently rain, and the effective overlap of the field as a whole increases. These long events are also frequently accompanied with a stratiform cloud mode below the inversion, marked by a shift in the height at which the hydrometeor frequency maximizes from 1 to 2 km. This was seen in the quick look in Figure 2, where between 1000 and 1130 UTC vigorous cumuli are accompanied with stratiform cloud near their tops. Such a scene as seen from space is the Advanced Spaceborne Thermal Emission and Reflection Radiometer (ASTER) image in Figure 6, taken about 10° east of Barbados, where shallow and somewhat deeper cumuli with tops near 3–4 km alternate with stratiform outflow. For long events, the percentage of entities with all cbh^1 located beyond 1.5 km, such as would be the case for an isolated stratiform cloud entity, has decreased to 27%, and hints that the stratiform cloud mode is often indeed connected to cumulus clouds, where the cumulus-under-stratiform cloud entity as a whole has its minimum cbh^1 below 1 km.

It is worthwhile mentioning one particular aspect that jumps out when having typical LES profiles of cloud fraction in mind while viewing Figures 4 and 5. For instance, the frequently used BOMEX (Barbados Oceanographic and Meteorological Experiment) and RICO LES runs (Siebesma *et al.*, 2003; Van Zanten *et al.*, 2011) show a faster exponential decrease of cloud fraction above 1 km than the radar profile in Figure 4. One explanation is that the BOMEX and RICO cases are biased towards a cloud regime that has more short cloud events such as shown in Figure 5(a). The simulations may also be performed on model domains that are too small to support the organization of clouds into larger clusters with significant outflow near 1.5–2 km, although the RICO profile hints at a second cloud peak near 1.5–2 km. Lastly, it is not unlikely that LES (too) quickly gets rid of smaller cloud patches because numerical diffusion limits the representation of processes occurring in regions of sharp gradients, such as near cloud edges or near the stable layer which tops the cloud layer.

What does the change in character of short to long cloud events imply for cloud cover CC and its contribution of CC_{LCL} versus CC_{ALOFT} ? A similar analysis is applied to the ceilometer distribution of cbh^1 , where the cloud duration is

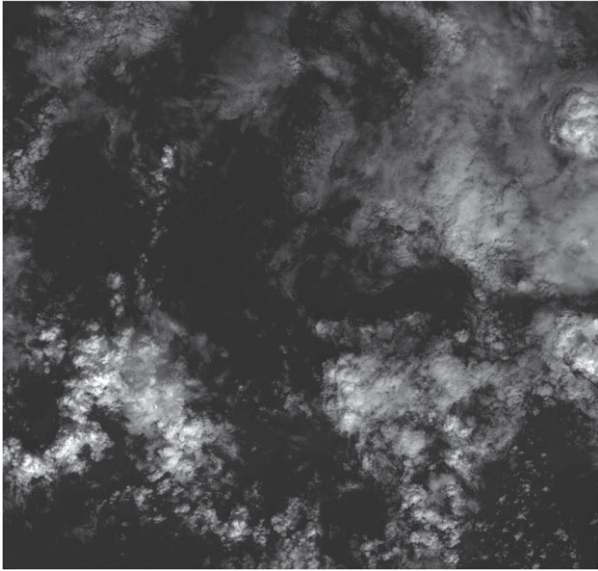


Figure 6. Scene from the Level 1B Product of ASTER taken between 13.2 and 13.8°N, 49.9 and 50.7°W on 10 December 2011 1354 UTC with the visible channel 1. Spatial resolution is 15 m.

defined as the period during which either cloud or rain is observed overhead at heights < 4 km (Figure 7). The relative frequencies can be summed up to provide CC_{LCL}^* , CC_{ALOFT}^* and rain cover RC^* , which altogether make up 1. The asterisk is included to indicate that these are cloud and rain covers relative to the total length of cloudy sky, and not the cloudy plus clear sky to which CC_{LCL} , CC_{ALOFT} and RC refer. The markers on the y -axis denote the most frequent, the median and the 90th percentile of cbh^1 . It shows that many of the changes in cloud character previously seen from the radar can be inferred from the distribution of cbh^1 alone, most notably the shift towards deeper cloud, more rain, and more stratiform outflow that causes an upward shift of cbh^1 and a second peak near 2 km, overall increasing the relative contribution of CC_{ALOFT}^* . Here one should remember that, even when the minimum cbh^1 of an entity is below 1 or 1.5 km, edges of stretched clouds will be apparent at higher altitudes and vertically pointing instruments will identify these as a cbh^1 aloft, more so when the cloud is much deeper, irregular or connected to stratiform outflow. Because parameters such as CC_{LCL} , CC_{ALOFT} , the cloud duration and distribution of cbh^1 represent changes in the nature of the cloud field reasonably well, and are available for two years, they are used again in the time series in section 4 where seasonal variations in cloudiness are addressed.

3.4. Variance across temporal scales

Before doing so, we turn to one last question that we would like to answer using the radar data: at what heights is the cloud field most variable and on what time-scales? As one might expect from the previous figures, but what may have not been anticipated beforehand, is that most of the variance in cloud is located near 2 km (Figure 4(b) on the left), where we applied spectral analysis on the cloud time series at each individual height using the longest continuous vertical pointing mode of the radar, from early January to the end of March 2012. The contour values correspond to the raw variance spectra, where time-scales beyond five days are excluded because these are less meaningfully interpreted when the time record is just 90 days. The highest variance peaks generally occur at heights between 1 and 2 km and on longer time-scales. The solid black line overlying the contour plot corresponds to the time-scale that explains 50% of the total variance, which is about 3 h for heights below 1 km and more than 6 h for heights near 2 km.

Overall the variability in cloud at heights aloft is thus larger than variability in cloud near the LCL (Figure 4(b), on the right). The variability at heights near 2 km is related to the second mode of stratiform-like cloud and is more pronounced on longer time-scales. It also varies fairly independently from cloud near the LCL and the covariance between those two components is poor (not shown).

Using the longer record of the ceilometer data, the same spectral analysis is applied to different components of total projected cloud cover, plotted in Figure 8. Rather than the raw variance spectra, the cumulative variance is plotted, summed from short to longer time-scales. As an example, 50% of the total variance in CC_{LCL} is contained on time-scales less than 6 h, whereas CC_{ALOFT} and RC reach that 50% only after including time-scales up to 12 h and more than 1 day respectively. In other words, the cloud cover contribution from cloud near the LCL contains more variance on shorter temporal scales than CC_{ALOFT} and RC , similar to what the radar shows.

Given the different mechanisms that play a role in controlling cloud at different heights, this difference in variance distribution can be explained. The deepening and spreading of clouds is controlled by factors such as large-scale subsidence or the strength of the vertical stratification at cloud top that vary on larger spatial and longer temporal scales than the sub-cloud layer (thermo-) dynamics that control cloud near the LCL. The explanation for the absence of long-time-scale variability in cloud near the LCL lies in the so-called cumulus valve mechanism (Albrecht *et al.*, 1979; Neggers *et al.*, 2006; Fletscher and Bretherton,

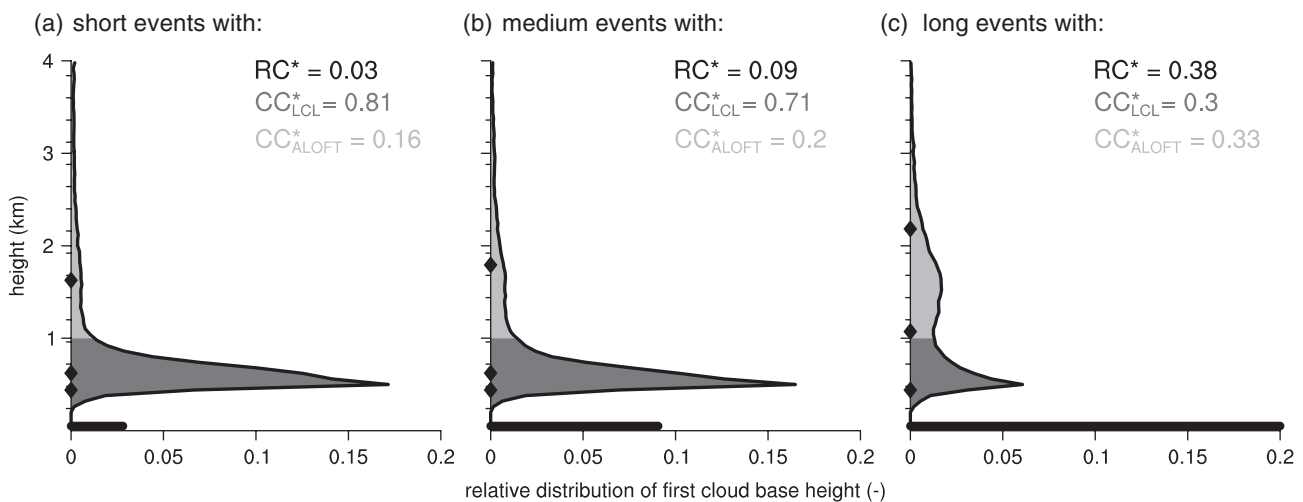


Figure 7. The vertical distribution of ceilometer cbh^1 relative to the total duration of cloudy sky, for cloud passages (a) < 3 min (contributing 23% to the total length of cloudy sky), (b) 3–12 min (35%) and (c) > 12 min (42%). The percentages are different from the radar, because the period of continuous vertical scanning is much longer for the ceilometer. The diamond markers on the y -axis indicate, from lowest to highest marker, the height of the maximum frequency, the median cbh^1 and the 90th percentile of cbh^1 . Colours are as in Figure 3.

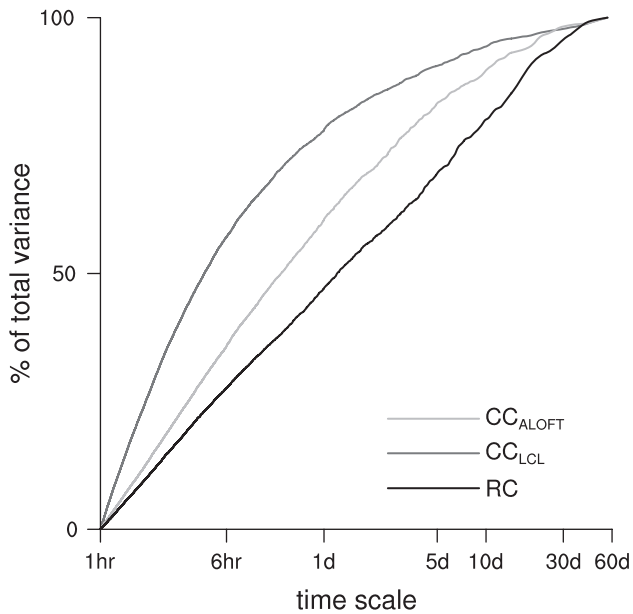


Figure 8. The cumulative sum of the normalized variance in CC_{LCL} (bold dark grey line), in CC_{ALOFT} (bold light grey) and RC (black) as a function of time-scale derived from two years of ceilometer cloud fraction and MRR rain fraction. Normalization is done using the total variance in each time series. Cumulative summation is done from short to long time-scales.

2010) whereby cloud activity itself acts as a regulator on moist convective transport. Not only does the height and strength of the transition layer atop the well-mixed sub-cloud layer regulate cloud formation, clouds themselves also influence the transition layer. By removing mass from the well-mixed sub-cloud layer, the transition layer height is lowered. At the same time, by

transporting moist air out of the sub-cloud layer and mixing drier and warmer air from the free troposphere downward, the LCL is raised. Combined, these act to limit convection, so that extensive cloud formation cannot be sustained for a long period of time. Similarly, periods with very little cloud amount also do not last for a long period of time, because in the absence of convective transport, an increase in sub-cloud layer humidity will lower the LCL below the transition layer and in turn promote cloud formation. This negative feedback mechanism ensures that sub-cloud layer thermodynamics approach equilibrium quickly, with time-scales between a couple of hours to a day (Bellon and Stevens, 2013), which constrains cloud amount near cloud base.

4. Seasonal cycle of cloudiness

In this last section, the previous findings on the distribution and variance of cloud at various height levels are used to explain the seasonality of low-level cloudiness. From 2010 to 2012, Barbados experienced both subsiding and rising large-scale motion, as measured by $\bar{\omega}$ at 700 hPa derived from ERA-Interim data averaged over a 5×5 degree area just upstream of Barbados (Figure 9(d)). On average the mean large-scale motion is ascent, $\bar{\omega} < 0$. The change in sign of $\bar{\omega}$ is related to the northward shift of the ITCZ during summer, and roughly separates the NH winter and spring (shaded grey), which lasts from December to May, from the NH summer and autumn, in a 12-year climatology from ERA-Interim (Brück, 2013). Compared to the climatology, the years 2010 and 2011 are overall more convective. For instance the spring and summer of 2010 are marked by anomalously southeasterly flow that brought more deep convective events to Barbados; also at the end of October 2010 a hurricane passed the site, and the winter months appear to have more convective events

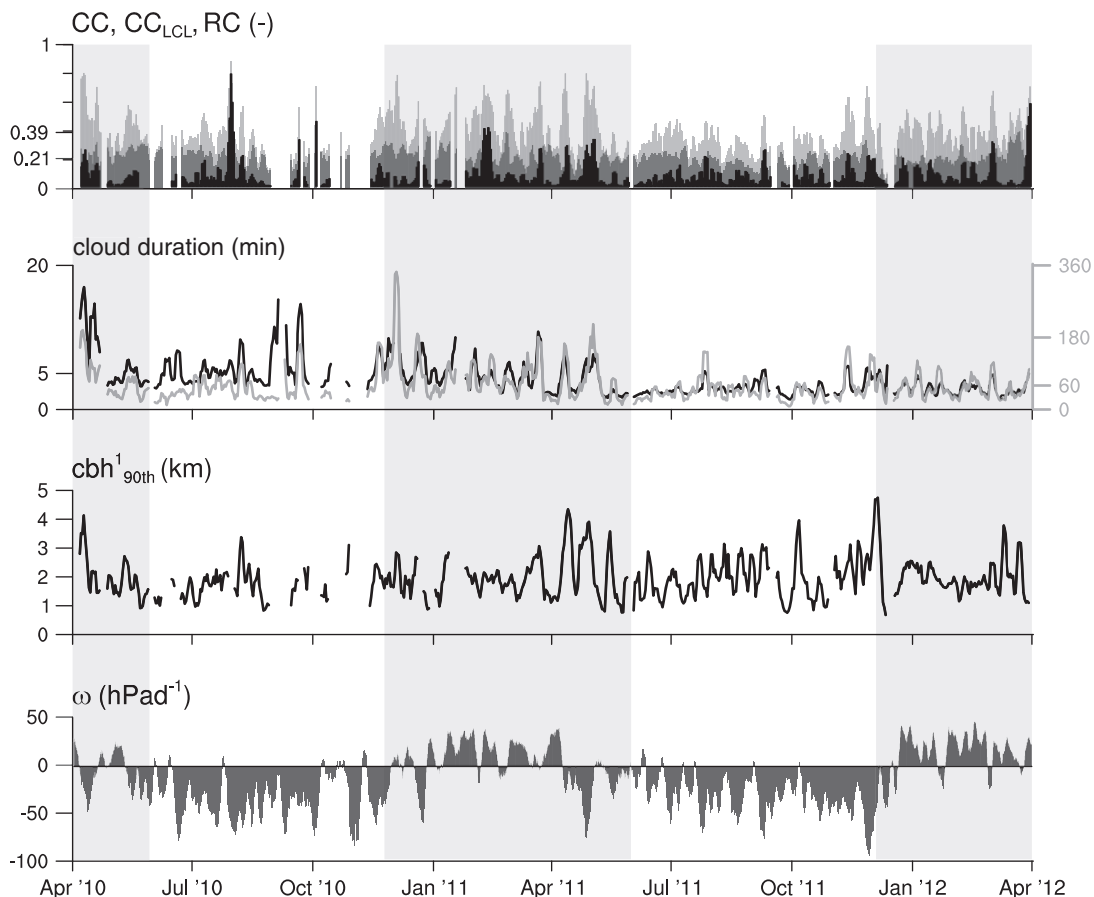


Figure 9. Two-year time series of (a) daily cloud cover CC (light grey) from the ceilometer, its contribution from cloud below 1 km CC_{LCL} (dark grey) and from rain RC (black); (b) the maximum (grey, right axis) and mean cloud duration (black, left axis); (c) the 90th percentile of the distribution of cbh^1 ; and (d) the large-scale vertical motion $\bar{\omega}$ at 700 hPa from ERA-Interim, taken as an average over a 5×5 degree grid box upstream of Barbados. The winter and spring season during which the climatology predicts subsiding motion are shaded grey. For all times when CC equals zero, the ceilometer was not operating.

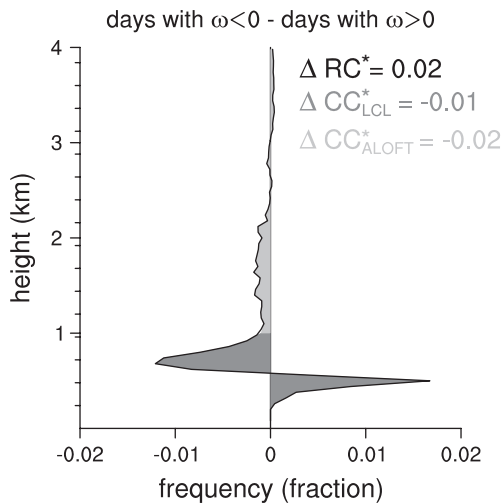


Figure 10. The difference in the relative distribution of first detected cloud-base height (as in Figure 7) between days with large-scale rising motion $\bar{\omega} < 0$ and days with large-scale subsiding motion $\bar{\omega} > 0$. ΔRC^* for instance means the difference in the relative contribution of RC^* to the total length of cloudy sky.

than usual. The winter and summer seasons are often referred to as the dry and the wet season because of the differences in rain they receive. However in terms of rain fraction RC , it is hard to distinguish the dry and wet season in Figure 9. This is likely because even shallow cumuli with tops below 3 km are raining frequently (Short and Nakamura, 2000; Lau and Wu, 2003; Nuijens *et al.*, 2009), so that a few isolated deep convective events with much higher rain-rates probably do not have a strong fingerprint on RC compared to the more frequent shallow rain events.

The two-year time series of daily cloud cover from the ceilometer is shown in Figure 9(a). The top edge of the light grey shading represents the total cloud cover CC from non-raining and raining cloud, which is the sum of CC_{LCL} , CC_{ALOFT} and RC . The top edge of the dark grey shading represents CC_{LCL} only and the black shading represents RC . Two points stand out in this time series: first, CC has more frequent high peak values during winter than during summer, and second, CC_{LCL} is on average 21%, and although variations around that value are present, they tend to be rather small compared to variations in RC and CC_{ALOFT} . For instance, there are hardly any days on which CC_{LCL} goes to zero and clouds are completely absent (note that the white gaps in the time series are simply due to missing data records).

Some peaks in wintertime CC are evidently related to peaks in RC (e.g. early February 2011 or end of April 2011) and presumably related to the passage of disturbances, but on average the higher CC during winter is due to the higher values of CC_{ALOFT} . These high CC_{ALOFT} cases are related to the passage of stratiform cloud, as seen in Figures 5 and 7, likely due to somewhat stronger inversions (Brück, 2013). The mean and maximum cloud duration (Figure 9(b)) confirm that peaks in CC_{ALOFT} are related to longer overpass times of clouds and that the mean cloud duration during winter is overall somewhat larger than during summer. This increase is not caused by a weakening of the winds, i.e. weaker winds would lengthen the overpass time of clouds. The winter in fact is marked by stronger winds, so if anything the seasonality in the winds should have diminished, rather than amplified, the differences in cloud duration seen here. Separating days by the mean wind shear, also derived from ERA-Interim for an area upstream of Barbados, further shows that the slanting of clouds does not explain peaks in cloud cover (not shown), presumably because the cloud overlap even in a low shear environment is already quite low (Brown, 1999; Neggers *et al.*, 2011).

The depth of the cloud field in Figure 9(c) is measured using the mean 90th percentile of cbh^1 , introduced earlier in the last paragraph of section 3.3. Seasonality in cbh^1_{90th} is not very evident

and it seems true that the depth of the cloud field peaks when ω is large and negative, whether that occurs during summer or winter. For instance, note the increase in cbh^1_{90th} at the beginning of April 2010, in April and May 2011, and in December 2011. High cloud cover days thus seem to occur when the cloud field as a whole is more convective, with deeper clouds and with a more pronounced stratiform cloud mode.

If, instead of contrasting winter versus summer periods, days with large-scale rising or subsiding motion are contrasted, it is confirmed that days with mean subsiding motion, which occur more frequently during winter, have relatively more cloud aloft contributing to cloud cover. Figure 10 plots the relative distribution of cloud-base heights for days with mean large-scale rising motion (from ERA-Interim) minus days with mean subsiding motion, which shows that days with mean rising motion have a larger contribution of rain events to cloud cover ($\Delta RC^* > 0$) at the expense of cloud aloft ($\Delta CC^*_{ALOFT} < 0$). Because relative humidity during summer is higher and the LCL lower, the distribution of cbh^1 is shifted downward, as evident from the positive peak in frequency below 600 m and the negative peak above 600 m. However, the total contribution of cbh^1 below 1 km to CC (CC^*_{LCL}) is not very different between the two seasons. In other words, lowering the LCL does not imply that the amount of cloud that forms near the LCL will have a larger contribution to cloud cover.

An explanation for why CC_{LCL} varies little throughout the seasons is the fast equilibrium time-scale and cumulus valve mechanism which is described at the end of the previous section. The cumulus valve mechanism apparently acts throughout a whole range of large-scale conditions: both subsiding and rising motion is experienced, as well as strong and weak winds, large and small surface fluxes, and variability in many other parameters. Although the extent to which these dynamics hold true across a range of atmospheric states still needs to be further explored, we may hypothesize that the sensitivity of cloud near the LCL in trade-wind-like locations is small. Changes in the total cloud amount in the trades may thus be limited to changes in the amount of cloud aloft.

5. Conclusions

The clouds observed on the east coast of Barbados (13°N, 59°W) have formed in air masses that have been transported by easterly winds from the west coast of northern Africa over a distance of ≈ 5000 km across the Atlantic into the deeper trades. Although the cloud field consists predominantly of shallow trade-wind cumuli, it has a rich character, reflecting variability in large-scale meteorology, local heterogeneity and the degree of cloud organization. Within a couple of hours, fields of cumuli can look remarkably different, in terms of how numerous, deep and large they are, whether they are raining, and whether they are accompanied by a second stratiform-like mode of cloud (Figure 6).

A two-year record of vertically pointing ground-based remote-sensing data are used in this study to characterize the distribution of low-level cloud in the trades (< 4 km), its contribution to cloud cover and its variability:

1. The total cloud cover of about 0.3 is dominated by non-raining cloud of which the first detected cloud base is located near the lifting condensation level (LCL). These contributions sum up to a cloud cover of 0.2.
2. Cloud with its first detected cloud base located further aloft (> 1 km) contributes an additional 0.1 to the total cloud cover. These contributions come from stratiform cloud, but also from edges of clouds that are irregular or sheared, an effect that gets more pronounced as clouds deepen, and from decaying clouds that have separated from their base.
3. The contribution of non-raining cloud near the LCL varies remarkably little across the wide range of large-scale conditions experienced on Barbados.

4. Variability in the contribution of cloud aloft and raining cloud is instead much more pronounced and appears to act independently of cloud near the LCL. This variability is mainly associated with a stratiform cloud mode near 1.5–2 km, even in regions this far into the trades, and with variability in the depth of the cloud field.
5. The total cloud cover is higher during the winter season when large-scale motion is downward and stratiform-like cloud is favoured in the presence of higher stability. During summer, when large-scale motion is upward, clouds are on average deeper and the relative contribution of raining cloud to total cloud cover is increased.

That cloudiness near cloud base is fairly constant across a range of conditions can be explained by the cumulus valve mechanism. This mechanism regulates the degree of convective transport of moisture and mass out of the sub-cloud layer, and imposes a negative feedback that effectively keeps the top of the mixed-layer close to cloud-base height. It ensures that the sub-cloud layer equilibrates quickly and constrains sub-cloud layer thermodynamics, and thereby cloudiness near the LCL (Neggers *et al.*, 2006; Bellon and Stevens, 2013).

The more tenuous and fragmented cloud near the LCL is on average the largest contributor to the total cloud cover – about two-thirds. Even when these optically thinner clouds are excluded, and the cloud field is more dominated by thicker raining cloud and stratiform cloud aloft, the contribution of cloud near the LCL is rarely less than a half. Because this part of the cloud field does not systematically vary, it is hypothesized that reductions in total cloud cover in the trades in response to changes in meteorology or climate are limited to its smaller contribution from cloud aloft.

Acknowledgements

Many thanks go to Friedhelm Jansen, Bjorn Brüggmann, Holger Linné, and Monika Pfeiffer for their invaluable help in setting up and maintaining the Observatory and in providing a data transfer and storage infrastructure. Without their efforts none of this work would have been possible. We thank Heiner Matthias Brück for providing the ERA-Interim data and Thorsten Mauritsen and Cathy Hohenegger for their constructive comments on an earlier draft. The comments of three reviewers greatly helped improve the final version of the manuscript. The ASTER L1B scene was obtained through the online Data Pool at the NASA Land Processes Distributed Active Archive Center (LP DAAC), USGS/Earth Resources Observation and Science (EROS) Center, Sioux Falls, South Dakota (https://lpdaac.usgs.gov/get_data) and Katrin Lonitz thanks Leon Maldonado for his help in the ordering and processing of ASTER data.

Appendix

Dependence of cloud cover on chosen thresholds

Cloud cover or cloud fraction are poorly defined quantities and hard to constrain from observations. Each instrument has its own measurement technique and sensitivity to detect cloud and, depending on one's choice of threshold to define what is cloud, a range of cloud fractions can be derived. In Figure A1, we demonstrate the sensitivity of cloud cover derived from the cloud radar and Raman lidar to our choice of threshold, and discuss what this implies for our conclusions on how different parts of the cloud field contribute to total cloud cover. Here we distinguish between cloud cover contributions from cloud below 1 km (CC_{LCL}) and from cloud above 1 km (CC_{ALOFT}), first introduced in section 3.1.

In general, the lidar sees less cloud aloft because of its low temporal resolution of 2 min, so that very thin cloud or irregular edges of cloud are easily missed, and therefore the relative contribution of CC_{ALOFT} to CC is smaller. By decreasing the

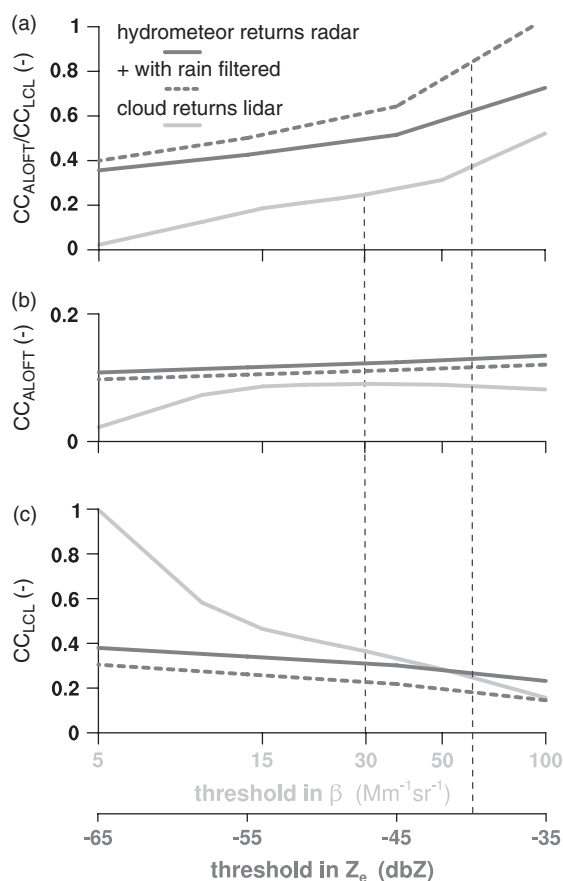


Figure A1. Dependence of (c) CC_{LCL} , (b) CC_{ALOFT} and (a) the ratio CC_{ALOFT}/CC_{LCL} to (i) choice of particle backscatter threshold $\log \beta$ for the lidar (light gray) and (ii) choice of reflectivity threshold Z_e for the radar, where the solid and dashed dark grey lines correspond to the hydrometeor returns and returns that exclude significant rain (Figure 4 – and its discussion in the text). Note that the two x-axes (for β and Z_e) are independent, i.e. $\beta = 5 Mm^{-1}sr^{-1}$ does not necessarily correspond to $Z_e = -65$ dBZ.

threshold of either β or Z_e , more optically thin cloud will be included and CC_{LCL} increases. In comparison, CC_{ALOFT} is fairly insensitive to a change in threshold, in particular for the radar. This is due to the increase of reflectivity with height inside clouds, due to the increase in liquid water content and cloud droplet sizes. Cloud detections at heights beyond 1 km are expected to have Z_e values well beyond -35 dBZ, or β values beyond $100 Mm^{-1}sr^{-1}$. Stratus-like layers, when present aloft, are also more likely to be optically thick.

CC_{LCL} is more sensitive to changing the threshold, in particular for the lidar, where at low β returns from aerosol are included, so that an apparent cloud cover of 1 is reached for $\beta = 5 Mm^{-1}sr^{-1}$. That CC_{ALOFT} in fact increases when raising the threshold, is because removing cloud at heights below 1 km, which decreases CC_{LCL} , may expose part of the cloud beyond 1 km, which then instead contributes effectively to cloud cover. Especially for the radar, that effect is very small, implying that CC_{ALOFT} is rather independent of CC_{LCL} .

CC_{ALOFT} is a factor 1.25 smaller than CC_{LCL} when considering a non-raining cloud field at a Z_e threshold of about -40 dBZ (the dashed dark grey in Figure A1(a)). When including raining cloud (solid dark grey), CC_{LCL} effectively increases and CC_{ALOFT} becomes a factor of 2 smaller than CC_{LCL} . The same decrease in the contribution of CC_{ALOFT} to total CC is achieved by lowering the Z_e threshold to more realistic values or looking at the lidar values instead, both of which are equivalent to including more optically thin cloud. In general however, across a range of thresholds, the dominant contributor to CC remains cloud near the LCL, whether as optically thin shallow cloud or as thicker raining cloud.

References

- Ahlgrimm M, Kohler M. 2010. Evaluation of trade cumulus in the ECMWF model with observations from CALIPSO. *Mon. Weather Rev.* **138**: 3071–3083.
- Albrecht B, Betts AK, Schubert W, Cox S. 1979. A model of the thermodynamic structure of the trade-wind boundary layer. Part I: Theoretical formulation and sensitivity tests. *J. Atmos. Sci.* **36**: 73–89.
- Augstein E, Riehl H, Ostapoff F, Wagner V. 1973. Mass and energy transports in an undisturbed Atlantic trade-wind flow. *Mon. Weather Rev.* **101**: 101–111.
- Bellon G, Stevens B. 2013. Timescales of the trade-wind boundary-layer adjustment. *J. Atmos. Sci.* **70**: 1071–1083.
- Bony S, Dufresne JL. 2005. Marine boundary-layer clouds at the heart of tropical cloud feedback uncertainties in climate models. *Geophys. Res. Lett.* **32**: L20806. doi: 10.1029/2005GL023851.
- Brown AR. 1999. Large-eddy simulations and parametrization of the effects of shear on shallow cumulus convection. *Boundary-Layer Meteorol.* **91**: 65–80.
- Brück HM. 2013. 'On the seasonal cycle of the North Atlantic trades and its clouds', Master's thesis, University of Hamburg; Germany.
- Comstock KK, Wood R, Yuter SE, Bretherton CS. 2004. Reflectivity and rain rate in and below drizzling stratocumulus. *Q. J. R. Meteorol. Soc.* **130**: 2891–2918.
- Fletscher JK, Bretherton CS. 2010. Evaluating boundary layer-based mass flux closures using cloud-resolving model simulations of deep convection. *J. Atmos. Sci.* **67**: 2212–2225.
- Hinkelman L, Stevens B, Evans K. 2005. A large-eddy simulation study of anisotropy in fair-weather cumulus cloud fields. *J. Atmos. Sci.* **62**: 2155–2171.
- Johnson RH, Lin X. 1997. Episodic trade wind regimes over the western Pacific warm pool. *J. Atmos. Sci.* **54**: 2020–2034.
- Lau KM, Wu HT. 2003. Warm rain processes over tropical oceans and climate implications. *Geophys. Res. Lett.* **30**: 2290. doi: 10.1029/2003GL018567.
- Leahy L, Wood R, Charlson R, Hostetler C, Rogers R, Vaughan M, Winker DM. 2012. On the nature and extent of optically thin marine low clouds. *J. Geophys. Res.* **117**: D22201. doi: 10.1029/2012JD017929.
- Malkus JS, Riehl H. 1964. Cloud structure and distributions over the tropical Pacific Ocean. *Tellus* **16**: 275–287.
- Marchand R, Ackerman T, Smyth M, Rossow WB. 2010. A review of cloud top height and optical depth histograms from MISR, ISCPP, and MODIS. *J. Geophys. Res.* **115**: D16206. doi: 10.1029/2009JD013422.
- Matheou G, Chung D, Nuijens L, Stevens B, Teixeira J. 2010. On the fidelity of large-eddy simulation of shallow precipitating cumulus convection. *Mon. Weather Rev.* **138**: 2918–2939.
- Medeiros B, Stevens B. 2011. Revealing differences in GCM representations of low clouds. *Clim. Dyn.* **36**: 385–399.
- Medeiros B, Nuijens L, Antoniazzi C, Stevens B. 2010. Low-latitude boundary-layer clouds as seen by CALIPSO. *J. Geophys. Res.* **115**: D23207. doi: 10.1029/2010JD014437.
- Neggers RAJ, Stevens B, Neelin JD. 2006. A simple equilibrium model for shallow-cumulus-topped mixed layers. *Theor. Comput. Fluid Dyn.* **20**: 305–322.
- Neggers RAJ, Heus T, Siebesma AP. 2011. Overlap statistics of cumuliform boundary-layer cloud fields in large-eddy simulations. *J. Geophys. Res.* **116**: D21202. doi: 10.1029/2011JD015650.
- Nuijens L, Stevens B, Siebesma AP. 2009. The environment of precipitating shallow cumulus convection. *J. Atmos. Sci.* **66**: 1962–1979.
- Qian Y, Long CN, Comstock JM, McFarlane SA, Xie S. 2012. Evaluation of cloud fraction and its radiative effects simulated by IPCC AR4 global models against ARM observations. *Atmos. Chem. Phys.* **12**: 1785–1810.
- Rauber RM, Ochs III HT, Di Girolamo L, Göke S, Snodgrass E, Stevens B, Knight C, Jensen JB, Lenschow DH, Rilling RA, Rogers DC, Stith JL, Albrecht BA, Zuidema P, Blyth AM, Fairall CW, Brewer WA, Tucker S, Lasher-Trapp SG, Mayol-Bracero OL, Vali G, Geerts B, Anderson JR, Baker BA, Lawson RP, Bandy AR, Thornton DC, Burnet E, Brenguier J-L, Gomes L, Brown PRA, Chuang P, Cotton WR, Gerber H, Heikes BG, Hudson JG, Kollias P, Krueger SK, Nuijens L, O'Sullivan DW, Siebesma AP, Twohy CH. 2007. Rain in (shallow) cumulus over the ocean – the RICO campaign. *Bull. Am. Meteorol. Soc.* **88**: 1912–1928.
- Remillard J, Kollias P, Luke E, Wood R. 2012. Marine boundary-layer cloud observations in the Azores. *J. Clim.* **25**: 7381–7398.
- Short DA, Nakamura K. 2000. TRMM radar observations of shallow precipitation over the tropical oceans. *J. Clim.* **13**: 4107–4124.
- Siebesma AP, Bretherton CS, Brown A, Chlond A, Cuxart J, Duynkerke PG, Jiang HL, Khairoutdinov M, Lewellen D, Moeng CH, Sanchez E, Stevens B, Stevens DE. 2003. A large-eddy simulation intercomparison study of shallow cumulus convection. *J. Atmos. Sci.* **60**: 1201–1219.
- Slingo J. 1978. The development and verification of a cloud prediction scheme for the ECMWF model. *Q. J. R. Meteorol. Soc.* **104**: 899–927.
- Stevens B, Ackerman AS, Albrecht BA, Brown AR, Chlond A, Cuxart J, Duynkerke PG, Lewellen DC, Macvean MK, Neggers RAJ, Sánchez E, Siebesma AP, Stevens DE. 2001. Simulations of trade wind cumuli under a strong inversion. *J. Atmos. Sci.* **58**: 1870–1891.
- Sui CH, Lau KM, Takayabu YN, Short DA. 1997. Diurnal variations in tropical oceanic cumulus convection during TOGA COARE. *J. Atmos. Sci.* **54**: 639–655.
- Van Zanten MC, Stevens B, Nuijens L, Siebesma AP, Ackerman A, Bogenschutz P, Burnet F, Cheng A, Couvreur F, Jiang H, Khairoutdinov M, Lewellen DS, Noda A, Mechem D, Shipway B, Slawinska J, Wang S. 2011. Controls on precipitation and cloudiness in simulations of trade-wind cumulus as observed during RICO. *J. Adv. Model. Earth Syst.* **3**: M06001. doi: 10.1029/2011MS000056.
- Vial J, Dufresne JL, Bony S. 2013. On the interpretation of inter-model spread in CMIP5 climate sensitivity estimates. *Clim. Dyn.* **41**: 3339–3362. doi: 10.1007/s00382-013-1725-9.
- Xie S, McCoy RB, Klein SA, Cederwall RT, Wiscombe WJ, Jensen MP, Johnson KL, Clothiaux EE, Gaustad KL, Long CN, Mather JH, McFarlane SA, Shi Y, Golaz J-C, Lin Y, Hall SD, McCord RA, Palanisamy G, Turner DD. 2010. Clouds and more: ARM climate modeling best estimate data. *Bull. Am. Meteorol. Soc.* **91**: 13–20.
- Zhao H, Di Girolamo L. 2006. Cloud fraction errors for trade wind cumuli from EOS-Terra instruments. *Geophys. Res. Lett.* **33**: L20802. doi: 10.1029/2006GL027088.
- Zhao H, Di Girolamo L. 2007. Statistics on the macrophysical properties of trade wind cumuli over the tropical western Atlantic. *J. Geophys. Res.* **112**: D10204. doi: 10.1029/2006JD007371.